

University of Groningen

Kinetic mechanism of Na⁺-coupled aspartate transport catalyzed by GltTk

Trinco, Gianluca; Arkhipova, Valentina; Garaeva, Alisa; Hutter, C.A.J.; Seeger, M.A.; Guskov, Albert; Slotboom, Dirk

Published in:
 Communications biology

DOI:
[10.1038/s42003-021-02267-y](https://doi.org/10.1038/s42003-021-02267-y)

IMPORTANT NOTE: You are advised to consult the publisher's version (publisher's PDF) if you wish to cite from it. Please check the document version below.

Document Version
Version created as part of publication process; publisher's layout; not normally made publicly available

Publication date:
2021

[Link to publication in University of Groningen/UMCG research database](#)

Citation for published version (APA):

Trinco, G., Arkhipova, V., Garaeva, A., Hutter, C. A. J., Seeger, M. A., Guskov, A., & Slotboom, D. (2021). Kinetic mechanism of Na⁺-coupled aspartate transport catalyzed by GltTk. *Communications biology*, 4, [751]. <https://doi.org/10.1038/s42003-021-02267-y>

Copyright

Other than for strictly personal use, it is not permitted to download or to forward/distribute the text or part of it without the consent of the author(s) and/or copyright holder(s), unless the work is under an open content license (like Creative Commons).





The publication may also be distributed here under the terms of Article 25fa of the Dutch Copyright Act, indicated by the "Taverne" license. More information can be found on the University of Groningen website: <https://www.rug.nl/library/open-access/self-archiving-pure/taverne-amendment>.

Take-down policy

If you believe that this document breaches copyright please contact us providing details, and we will remove access to the work immediately and investigate your claim.

Downloaded from the University of Groningen/UMCG research database (Pure): <http://www.rug.nl/research/portal>. For technical reasons the number of authors shown on this cover page is limited to 10 maximum.

Kinetic mechanism of Na⁺-coupled aspartate transport catalyzed by Glt_{TK}

Gianluca Trinco¹, Valentina Arkhipova^{1,4}, Alisa A. Garaeva^{1,5}, Cedric A. J. Hutter ², Markus A. Seeger ², Albert Guskov ^{1,3} & Dirk J. Slotboom ¹✉

It is well-established that the secondary active transporters Glt_{TK} and Glt_{PH} catalyze coupled uptake of aspartate and three sodium ions, but insight in the kinetic mechanism of transport is fragmentary. Here, we systematically measured aspartate uptake rates in proteoliposomes containing purified Glt_{TK}, and derived the rate equation for a mechanism in which two sodium ions bind before and another after aspartate. Re-analysis of existing data on Glt_{PH} using this equation allowed for determination of the turnover number (0.14 s⁻¹), without the need for error-prone protein quantification. To overcome the complication that purified transporters may adopt right-side-out or inside-out membrane orientations upon reconstitution, thereby confounding the kinetic analysis, we employed a rapid method using synthetic nanobodies to inactivate one population. Oppositely oriented Glt_{TK} proteins showed the same transport kinetics, consistent with the use of an identical gating element on both sides of the membrane. Our work underlines the value of bona fide transport experiments to reveal mechanistic features of Na⁺-aspartate symport that cannot be observed in detergent solution. Combined with previous pre-equilibrium binding studies, a full kinetic mechanism of structurally characterized aspartate transporters of the SLC1A family is now emerging.

¹Groningen Biomolecular Sciences and Biotechnology Institute, University of Groningen, Groningen, The Netherlands. ²Institute of Medical Microbiology, University of Zurich, Zurich, Switzerland. ³Moscow Institute of Physics and Technology, Dolgoprudny, Russia. ⁴Present address: ZoBio BV, Leiden, The Netherlands. ⁵Present address: Institute of Medical Microbiology, University of Zurich, Zurich, Switzerland. ✉email: d.j.slotboom@rug.nl

Excitatory amino acid transporters (EAATs) of the solute carrier family 1A (SLC1A) take up the neurotransmitter L-glutamate from the synaptic environment, which is necessary to keep the extracellular concentration low and prevent neurotoxicity^{1,2}. EAATs couple uptake of one amino acid substrate molecule to the co-transport of three sodium ions and one proton and counter-transport of one potassium ion^{3–6}. Thus, glutamate gradients of a million-fold across the membrane under resting conditions can be sustained. The closely related archaeal transporters Glt_{Ph} from *Pyrococcus horikoshii* and Glt_{Tk} from *Thermococcus kodakarensis* of the SLC1A family (78% sequence identity to each other, ~36% sequence identity to EAATs) take up aspartate rather than glutamate in symport with three sodium ions and are not coupled to potassium or proton transport^{7–11}. These prokaryotic homologs of the neurotransmitter transporters have been instrumental in delineating shared structural features of this transporter family^{7–9,12–22}.

SLC1A family proteins are homotrimers, with independently operating protomers^{19,21,23–29}, each organized in two domains. A rigid scaffold domain mediates all the contacts with the neighboring protomers, and a peripheral transport domain binds the amino acid substrate and cations^{13,16,30,31}. The transport domains are mobile and move through the lipid bilayer (alike an elevator) when translocating the amino acid substrate and co-transported ions across the membrane¹³. During movement of the transport domain, the substrate-binding site is occluded from the solvent and shielded by the tips of two pseudo-symmetrical helical hairpins (HP1 and HP2). The latter hairpin is a gating element that can hinge between a closed position (taken during elevator movements) and an open position (allowing loading or release of the substrate and co-transported ions). The extent of the elevator-like movement of the transport domain is so large (~20 Å in Glt_{Tk}) that HP2 acts as a gating element both on the extracellular and the intracellular side of the membrane.

Transport assays in proteoliposomes have revealed that both Glt_{Ph} and Glt_{Tk} catalyze electrogenic transport with a strict stoichiometry of three co-transported Na⁺ ions per aspartate^{14,32}. Data from studies on equilibrium binding and pre-equilibrium kinetics of binding with the solubilized proteins in detergent solution have shown that co-transported ions and aspartate bind in a highly cooperative way, which is crucial to ensure thermodynamic coupling^{10,15,33–37}. These experiments have indicated that most likely two sodium ions bind first, then aspartate, and finally the third sodium ion. The binding of the last Na⁺ leads to gate closure of HP2, which in turn is a prerequisite for elevator-like conformational changes that translocate the bound cargo across the membrane. Structures of Glt_{Ph} and Glt_{Tk} have provided a qualitative explanation for the observed binding order. Two of the sodium binding sites (named Na1 and Na3) are buried deep in the proteins¹⁵. A substantial conformation rearrangement in the apo-protein (most pronounced in the conserved unwound region of TM7) is required to create the geometry needed for sodium binding, which makes this step slow. The conformational rearrangement, which is stabilized by the binding of the two sodium ions, also affects residues involved in aspartate binding. While the apo-state does not have a measurable affinity for aspartate, sodium binding creates a high-affinity site for the amino acid substrate. The last sodium ion binds to a site in direct contact with the HP2 gate (Na2), and locks the gate in the closed position, with aspartate and the three sodium ions occluded from the environment.

Despite the enormous amount of data on structure and binding mechanism in detergent solution, insight into the kinetic mechanism under translocating conditions is fragmented and incomplete. Here, we set out to determine the kinetic mechanism of aspartate transport by using purified Glt_{Tk} reconstituted in proteoliposomes. We measured initial rates of transport at a wide range of substrate and co-ion concentrations, a method that has been used extensively

for the mechanistic characterization of enzymes, leading to insight into the order of binding of substrates³⁸. This method has not been used much on purified membrane transporters, in part because it is often impossible to control the orientation of the reconstituted transporters in proteoliposomes, leading to mixed populations, thus complicating kinetic analysis.

To overcome this latter problem, we isolated an inhibitory synthetic nanobody³⁹, which we used to inactivate membrane transporters oriented in one of the two possible orientations. This method is rapid, generally applicable, and does not depend on mutagenesis and chemical modifications. The work presented here, combined with the results of previous pre-equilibrium binding studies³⁶, allows for the determination of accurate turnover numbers, which we illustrate by analyzing available data for aspartate transport by Glt_{Ph}.

Results

To study the kinetic mechanism of Na⁺-coupled aspartate transport by Glt_{Tk}, we used a classical enzymology method, in which we measured the initial uptake rates of radiolabelled L-aspartate into proteoliposomes reconstituted with purified Glt_{Tk}, as a function of the external concentrations of L-aspartate and Na⁺. To ensure initial rate conditions, aspartate and Na⁺ were absent from the lumen of the liposomes at the onset of the experiment, and the rate was determined from the linear part of the uptake experiment (Supplementary Fig. 1). In the first set of experiments (presented in Figs. 1–3 and Tables 1–3), we measured the combined transport activity of proteins with right-side-out and inside-out membrane orientation in the liposomes, as we did not inactivate either of the two populations. These experiments can be compared with binding experiments performed in detergent-solution where the sidedness is absent. In follow-up experiments (presented in Fig. 4 and Table 4), we silenced one of the two populations, which allows for comparison with experiments in which the transporters had been fixed in a single orientation by crosslinking^{35,36}.

We managed to determine accurate transport rates using external Na⁺ concentrations in the range between 5 and 300 mM and aspartate concentrations between 50 nM and 100 μM (Table 1). The upper and lower boundaries of the concentration ranges were set by practical considerations. Aspartate concentrations higher than 100 μM required large dilution of the radiolabelled amino acid with unlabeled aspartate, which caused poor signal-to-noise levels in the uptake experiments. Na⁺ concentrations higher than 300 mM could not be used, because the preparation of proteoliposomes in buffer containing high salt concentrations prevented the formation of a firm pellet when centrifuged, therefore making it impossible to reach the necessary protein concentration for the experiments. In the low concentration regime, conditions in which 1 mM Na⁺ was used in combination with aspartate concentrations lower than 1 μM resulted in poor signal-to-noise ratios. Despite these limitations, the range of concentrations was sufficient to provide insight into the kinetic mechanism.

The results of the uptake experiments in liposomes with mixed protein orientations are summarized in Table 1, where each row contains the initial rates of transport (v_0) at a fixed sodium concentration, but with increasing aspartate concentrations. When analyzing v_0 as a function of the aspartate concentration row-by-row, we found that rectangular hyperbolic functions fitted the data well (Fig. 1a), which allowed for the determination of the apparent maximal rates of transport (v_{max}^{Asp} (app)) and apparent Michaelis-Menten constants (K_M^{Asp} (app)) (Table 2). The superscript “Asp” indicates that the aspartate was varied, while the sodium concentration was kept constant (hence “apparent”).

Each column in Table 1 contains the measured initial rates of aspartate transport at increasing Na⁺ concentrations while

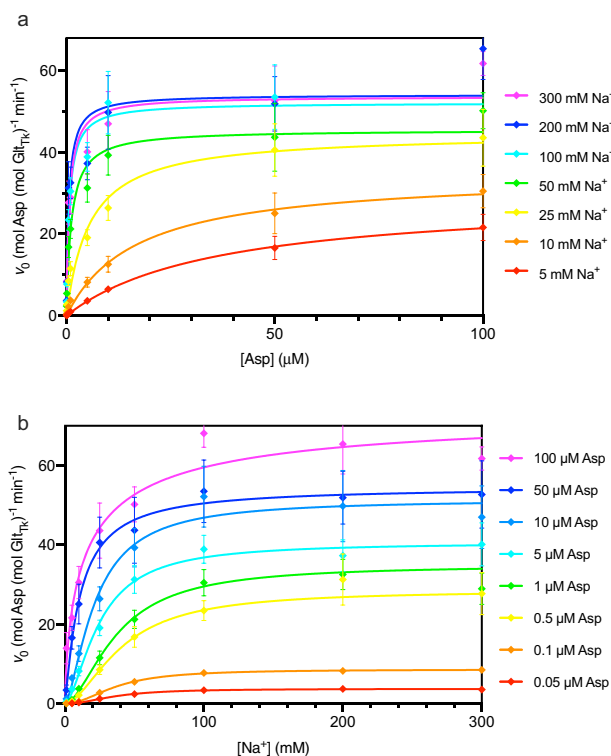


Fig. 1 L-Asp transport rates catalyzed by purified and reconstituted Glt_{T_R} as a function of the concentrations of Na⁺ and L-aspartate. The rates represent the combined contributions of right-side-out and inside-out oriented proteins. **a** Aspartate-dependent measurements at different fixed Na⁺ concentrations. The lines represent fits of the Michaelis-Menten equation to the data for uptake at Na⁺ concentrations of 5 mM (red), 10 mM (orange), 25 mM (yellow), 50 mM (green), 100 mM (cyan), 200 mM (blue), 300 mM (purple). **b** Sodium-dependence of transport at fixed L-Asp concentrations. The lines represent fits of the Hill equation to the data for uptake at 0.05 μM (red), 0.1 μM (orange), 0.5 μM (yellow), 1 μM (green), 5 μM (cyan), 10 μM (light blue), 50 μM (blue), 100 μM (purple). Each uptake rate represents the average of three independent biological replicates, each constituted by two technical replicates, and the standard error of the mean is shown.

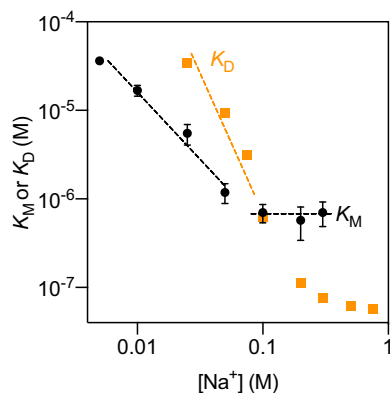


Fig. 2 Dependence of the apparent affinities for L-Asp (K_M^{ASP} (app)) on the sodium ion concentration (black symbols). Dashed lines represent linear fits to data points in the low and high sodium ion concentration regimes. Each value represents the average of three independent biological replicates, and two technical replicates. The standard error of the mean is shown. For comparison, the dissociation constants K_D^{ASP} (app) determined previously are also plotted (orange)¹⁵. The data represent the combined contributions of right-side-out and inside-out oriented proteins.

maintaining a fixed aspartate concentration. Analysis of these rates as a function of the Na⁺ concentration revealed sigmoidal dependencies (Fig. 1b). The Hill equation was used to fit the data, yielding values for v_{max}^{Na} (app) and K_M^{Na} (app) and the apparent Hill coefficient n_{Hill} (app) (Table 3). In this case, the superscript “Na” indicates sodium-dependent measurements, and “apparent” indicates that the measurements were done at a fixed L-aspartate concentration.

For interpretation of the uptake data in the framework of a kinetic model of transport, the apparent affinities for L-aspartate (K_M^{ASP} (app)) and the apparent maximal rates (v_{max}^{ASP} (app) and v_{max}^{Na} (app)) are the most informative parameters. K_M^{Na} (app) and n_{Hill} (app) contain less useful information for discrimination between different mechanisms (as discussed in references^{38,40}), and therefore these values were not used further here.

K_M analysis reveals a complex mechanism. Information on the kinetic mechanism is contained both in the dependence of the apparent affinity for aspartate K_M^{ASP} (app) on the Na⁺ concentration and in potential differences between K_M^{ASP} (app) and the equilibrium constant for L-aspartate binding (K_D^{ASP} (app)). Table 2 shows that K_M^{ASP} (app) was strongly dependent on the Na⁺ concentration at concentrations below 50 mM Na⁺. At Na⁺ concentrations above 100 mM, K_M^{ASP} (app) became independent of the Na⁺ concentration and leveled off to 0.7 μM (Table 2), a value that is important for mechanistic interpretation (discussed in detail below).

Comparison of the K_M^{ASP} (app) values with the equilibrium constants for L-aspartate binding (K_D^{ASP} (app)), determined previously by isothermal titration calorimetry (ITC) in detergent solution¹⁵, revealed almost identical values at a Na⁺ concentration of 100 mM, but large differences at higher and lower concentrations of Na⁺ (Fig. 2). While K_M^{ASP} (app) was an order of magnitude higher than the equilibrium constant for binding at a sodium concentration of 300 mM (7.0×10^2 nM versus 75 nM), at concentrations below ~75 mM, K_M^{ASP} (app) was up to an order of magnitude lower than the K_D^{ASP} (app). Such discrepancies are indicative of a complex kinetic mechanism that cannot be interpreted in the conceptual framework of the rapid equilibrium approximation, which is based on the assumption that the transport step (described by turnover number k_{cat}) is much slower than the establishment of the binding equilibrium of sodium ions and aspartate, described by the equilibrium constants K_D . The rapid equilibrium assumption was previously also dismissed for aspartate transport by Glt_{T_R}, based on a more limited comparison of K_M and K_D ¹⁰, and on pre-equilibrium binding experiments in detergent solution³⁶, but the data presented here, based on the comparison of transport and binding experiments over a broad range of sodium concentrations, revealed a variable ratio between K_M^{ASP} (app) and K_D^{ASP} (app) depending on the Na⁺ concentration, which is indicative of kinetic complexity. It is noteworthy that the rapid equilibrium assumption might hold at very low Na⁺ concentration³⁶, but as discussed above, the sensitivity of the radiolabel-based transport assays is not high enough to measure aspartate uptake in such conditions.

Mechanistic interpretation of transport data using the steady-state approximation. Because the rapid equilibrium approximation was found invalid, we turned to analysis based on the steady-state assumption. While the Michaelis–Menten or Hill equations can always describe the substrate dependencies of the uptake rates when the rapid equilibrium approximation is valid, it is possible to find more complex relations in the steady-state analysis, depending on the details of the kinetic mechanism³⁸. For instance, for some kinetic mechanisms, v_{max} values may be (local)

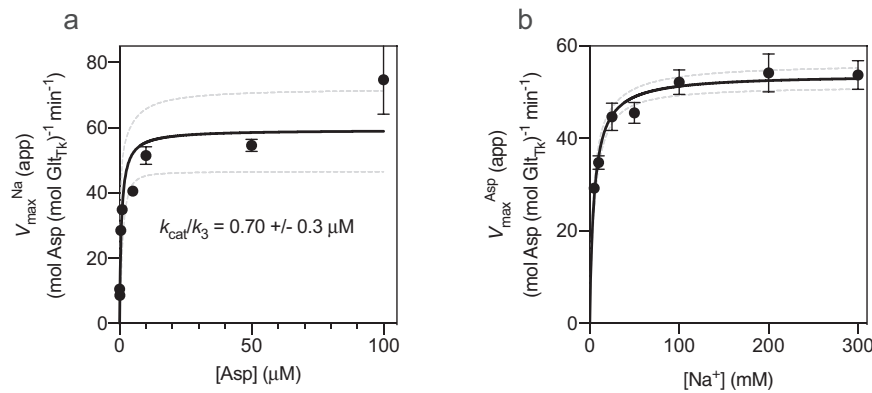


Fig. 3 Dependence of the maximal rates L-Asp transport rate on the concentrations of Na⁺ and L-aspartate. **a** Dependence of the maximal rates of transport v_{max}^{Na} (app) from Fig. 1a on the concentration of L-Asp. **b** Dependence of the maximal rates of transport v_{max}^{Asp} (app) from Fig. 1b on the concentration of sodium ions. Solid and dashed lines represent fits of rectangular hyperbolic functions to the data and the 95% confidence intervals, respectively. In panel A the fitted value of k_{cat}/k_3 (Eq. (13)) is indicated. Each value represents the average of three independent biological replicates, and two technical replicates. The standard error of the mean is shown. The data represent the combined contributions of right-side-out and inside-out oriented proteins.

Table 1 Initial rates of L-aspartate uptake by GlT_{TK} reconstituted in proteoliposomes. In the first column, the concentrations in parentheses indicate the amount of choline chloride used in the external reaction buffer to balance the osmotic and ionic strength. Each uptake rate represents the average of three independent biological replicates and independent reconstitutions, each with two technical replicates. The standard error of the mean is indicated.

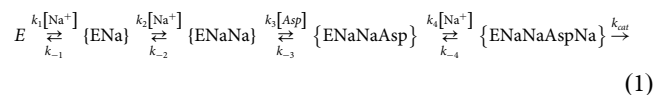
[L-Asp]→ [Na ⁺] ↓	0.05 μM	0.1 μM	0.5 μM	1 μM	5 μM	10 μM	50 μM	100 μM
1 mM (299 mM)	Not determined	Not determined	Not determined	0.03	0.51	0.25	2.85	10.93
5 mM (295 mM)	0.05	0.06	0.59	0.96	3.62	6.48	16.59	21.62
10 mM (290 mM)	± 1.6 10 ⁻² min ⁻¹	± 2.1 10 ⁻² min ⁻¹	± 0.1 min ⁻¹	± 0.2 min ⁻¹	± 0.7 min ⁻¹	± 0.9 min ⁻¹	± 2.8 min ⁻¹	± 3.2 min ⁻¹
25 mM (275 mM)	0.21	0.28	2.16	3.75	8.19	12.60	25.08	30.51
50 mM (250 mM)	± 5.5 10 ⁻² min ⁻¹	± 0.1 min ⁻¹	± 0.4 min ⁻¹	± 0.6 min ⁻¹	± 1.2 min ⁻¹	± 1.9 min ⁻¹	± 5.0 min ⁻¹	± 4.1 min ⁻¹
100 mM (200 mM)	0.95	1.46	8.53	11.56	19.09	26.39	40.58	43.59
200 mM (100 mM)	± 0.2 min ⁻¹	± 0.5 min ⁻¹	± 1.2 min ⁻¹	± 1.7 min ⁻¹	± 2.0 min ⁻¹	± 3.0 min ⁻¹	± 6.4 min ⁻¹	± 6.9 min ⁻¹
300 mM (0 mM)	1.88	3.34	16.79	21.26	31.28	39.30	43.69	50.21
	± 0.4 min ⁻¹	± 1.0 min ⁻¹	± 2.6 min ⁻¹	± 2.3 min ⁻¹	± 3.5 min ⁻¹	± 4.9 min ⁻¹	± 8.3 min ⁻¹	± 4.4 min ⁻¹
	2.75	4.79	23.46	30.47	38.90	52.16	53.52	68.13
	± 0.5 min ⁻¹	± 1.5 min ⁻¹	± 2.5 min ⁻¹	± 3.3 min ⁻¹	± 3.5 min ⁻¹	± 7.7 min ⁻¹	± 7.9 min ⁻¹	± 3.5 min ⁻¹
	3.06	4.83	31.27	32.55	37.29	49.80	51.90	65.40
	± 0.6 min ⁻¹	± 1.5 min ⁻¹	± 6.4 min ⁻¹	± 3.8 min ⁻¹	± 4.0 min ⁻¹	± 9.0 min ⁻¹	± 6.7 min ⁻¹	± 7.5 min ⁻¹
	2.93	4.96	27.72	28.95	40.12	46.98	52.69	61.77
	± 0.7 min ⁻¹	± 1.6 min ⁻¹	± 5.3 min ⁻¹	± 4.0 min ⁻¹	± 5.4 min ⁻¹	± 7.9 min ⁻¹	± 8.5 min ⁻¹	± 2.9 min ⁻¹

Table 2 v_{max}^{Asp} (app) and K_M^{Asp} (app) values for aspartate dependent uptakes obtained at constant [Na⁺].

[Na ⁺]	v_{max}^{Asp} (app) (min ⁻¹)	K_M^{Asp} (app) (μM)
5 mM	29.2 ± 0.58	36 ± 1.9
10 mM	34.8 ± 1.5	16.8 ± 2.4
25 mM	44.7 ± 2.9	5.5 ± 1.5
50 mM	45.5 ± 2.3	1.2 ± 0.3
100 mM	52.1 ± 2.6	0.70 ± 0.16
200 mM	54.2 ± 4.1	0.58 ± 0.23
300 mM	53.7 ± 3.1	0.70 ± 0.22

Values are derived from the data presented in Table 1 and Fig. 1a. Each uptake rate represents the average of three independent biological replicates, each with two technical replicates. The standard error of the mean is indicated.

initial rates are described well by rectangular hyperbola and sigmoidal curves (Figs. 1 and 2), suggesting that such random steps do not play a significant role, at least not in the concentration regime that we used. This notion is consistent with the kinetic binding model derived for detergent-solubilized GlT_{ph}, where the binding of sodium ions and aspartate to GlT_{ph} was found to be ordered in the concentration range between 5 and 300 mM Na⁺, with two sodium ions binding before and one after aspartate³⁶. This ordered binding mechanism is also consistent with a recent study that revealed a conformational selection step leading to the binding of the first sodium ion³⁴. Therefore, we chose to analyze the transport data presented here with the following kinetic model:



maxima, instead of being reached asymptotically, and K_M values may be undefined. Such complex relations often arise when steps occur in the mechanism where two different substrates (corresponding to aspartate and Na⁺ in the case of GlT_{TK}) bind randomly³⁸. In our data, the concentration dependences of the

in which E designates GlT_{TK}.

While we base our further analysis on the mechanism shown in Eq. (1), we will show in the discussion section that the main conclusions hold for any mechanism in which at least one sodium ion binds after aspartate.

Table 3 v_{max}^{Na} (app), K_M^{Na} (app) and n_{Hill} (app) values for Na^+ dependent uptakes obtained at constant [Asp].

[L-Asp]	v_{max}^{Na} (app) (min ⁻¹)	K_M^{Na} (app) (mM)	n_{Hill} (app)
0.05 μM	3.7 ± 0.1	36.7 ± 1.8	2.1 0.19
0.1 μM	8.6 ± 0.1	37.0 ± 0.81	2.0 ± 0.08
0.5 μM	28.5 ± 0.15	40.9 ± 0.42	1.70 ± 0.025
1 μM	34.9 ± 1.0	37.3 ± 2.0	1.7 ± 0.13
5 μM	40.6 ± 1.3	24.7 ± 2.1	1.6 ± 0.19
10 μM	51.4 ± 2.7	21.8 ± 3.2	1.5 ± 0.29
50 μM	54.6 ± 1.9	10.9 ± 1.2	1.1 ± 0.14
100 μM	72.34 ± 10.5	14.8 ± 7.9	0.72 ± 0.21

Values are derived from the data presented in Table 1 and Fig. 1b. Each uptake rate represents the average of three independent biological replicates, each with two technical replicates. The standard error of the mean is indicated.

Table 4 v_{max}^{Asp} (app) and K_M^{Asp} (app) values for aspartate dependent uptakes obtained at constant $[Na^+]$ in the presence of 750 nM sybody on the outside of the liposomes.

$[Na^+]$	v_{max}^{Asp} (app) (min ⁻¹)	K_M^{Asp} (app) (μM)
10 mM	9.8 ± 1.0	4.9 ± 1.4
100 mM	18.3 ± 2.0	0.97 ± 0.36
200 mM	17.0 ± 1.0	0.65 ± 0.13
300 mM	17.2 ± 1.5	0.63 ± 0.17

Each uptake rate represents the average of two independent biological replicates, each with two technical replicates. The standard error of the mean is indicated.

To derive a rate equation for this kinetic model of Eq. (1), we used the King-Altman method^{38,41}:

$$\frac{v_0}{v_{max}} = \frac{a_1[Na]^2[Asp]}{a_1[Na]^3[Asp] + a_2[Na]^2[Asp] + a_3[Na][Asp] + a_4[Na]^3 + a_5[Na]^2 + a_6[Na] + a_7} \quad (2)$$

in which v_{max} is the maximal attainable rate of transport at high Na^+ and L-aspartate concentrations, and a_1 – a_7 are expressions of rate constants:

$$a_1 = k_1k_2k_3k_4 \quad (3)$$

$$a_2 = k_2k_3k_4k_{cat} + k_1k_3k_4k_{cat} + k_1k_2k_3k_{cat} + k_1k_2k_3k_{-4} \quad (4)$$

$$a_3 = k_{-1}k_3k_4k_{cat} \quad (5)$$

$$a_4 = k_1k_2k_4k_{cat} \quad (6)$$

$$a_5 = k_1k_{-2}k_4k_{cat} + k_1k_2k_{-3}k_{cat} + k_1k_2k_{-3}k_{-4} \quad (7)$$

$$a_6 = k_1k_{-2}k_{-3}k_{cat} + k_{-1}k_{-2}k_4k_{cat} + k_1k_{-2}k_{-3}k_{-4} \quad (8)$$

$$a_7 = k_{-1}k_{-2}k_{-3}k_{cat} + k_{-1}k_{-2}k_{-3}k_{-4} \quad (9)$$

Equation (2) can be rearranged to derive expressions for v_{max}^{Na} (app) and v_{max}^{Asp} (app):

$$v_{max}^{Asp}(\text{app}) = v_{max} * \frac{a_1[Na]^2}{a_1[Na]^2 + a_2[Na] + a_3} \quad (10)$$

$$v_{max}^{Na}(\text{app}) = v_{max} * \frac{[Asp]}{\frac{a_4}{a_1} + [Asp]} = v_{max} * \frac{[Asp]}{\frac{k_{cat}}{k_3} + [Asp]} \quad (11)$$

Thus, the model predicts that both v_{max}^{Na} (app) and v_{max}^{Asp} (app) are dependent on the concentration of the other substrate, which is fully consistent with the data presented in Fig. 3a, b. Moreover, Eq. (11) describes a rectangular hyperbolic relation between v_{max}^{Na} (app) and [Asp]. By fitting the Michaelis-Menten equation to the data (Fig. 3a), we found a value for k_{cat}/k_3 of 0.7 μM. Since the turnover number k_{cat} is known from the v_{max} data ($\sim 0.9 \text{ s}^{-1}$ ($\sim 54 \text{ min}^{-1}$), see Fig. 3, Table 2), a value of $\sim 1.3 \times 10^6 \text{ M}^{-1} \text{ s}^{-1}$ for k_3 is derived, remarkably similar to the value of $1.2 \times 10^6 \text{ M}^{-1} \text{ s}^{-1}$ that was found for Glt_{ph} , obtained in pre-equilibrium binding experiments³⁶.

Equation (2) can also be rearranged to derive an expression for K_M^{Asp} (app):

$$K_M^{Asp}(\text{app}) = \frac{a_4[Na]^3 + a_5[Na]^2 + a_6[Na] + a_7}{a_1[Na]^3 + a_2[Na]^2 + a_3[Na]} \quad (12)$$

From Eq. (12) the values for K_M^{Asp} (app) that are reached in the low and high $[Na^+]$ regimes can be found:

$$\lim_{[Na] \rightarrow \infty} K_M^{Asp}(\text{app}) = \frac{a_4}{a_1} = \frac{k_{cat}}{k_3} \quad (13)$$

$$\lim_{[Na] \rightarrow 0} K_M^{Asp}(\text{app}) = \frac{a_7}{a_3[Na]} \quad (14)$$

Equation (13) predicts that in the high concentration limit a constant value for K_M^{Asp} (app) is reached, which equals the ratio between two rate constants k_{cat}/k_3 . The data presented in Fig. 2 and Table 2 show that the value of K_M^{Asp} (app) levels off to $\sim 0.7 \mu\text{M}$ at high Na^+ concentration. Since the turnover number k_{cat} is $\sim 0.9 \text{ s}^{-1}$ (Fig. 3 and Table 2), a value of $\sim 1.3 \times 10^6 \text{ M}^{-1} \text{ s}^{-1}$ for k_3 is found. Thus, two approaches (analysis of v_{max}^{Na} (app) and K_M^{Asp} (app)), reveal a value for k_3 that agrees well with the value of $1.2 \times 10^6 \text{ M}^{-1} \text{ s}^{-1}$ that was found for Glt_{ph} .

When the apparent affinity constants are plotted in a double logarithmic plot against the concentration of Na^+ , linear relations are approached in both the high and low Na^+ concentration extremes (Fig. 2). The slope is zero at high Na^+ concentration (because K_M^{Asp} (app) levels off to k_{cat}/k_3), and a slope of -1.4 is found in the low Na^+ concentration regime, which deviates from the slope of -1 predicted by the model. This discrepancy may indicate that lower concentrations of sodium should have been used to meet the conditions for Eq. (14) to be valid, something which was impossible for technical reasons, as discussed above. Alternatively, the deviation might be caused by the experimental error inherent to the transport measurements at low Na^+ concentrations. The slope of the $\log(K_M)$ plot in the low Na^+ concentration regime is approximately twofold shallower than that of the $\log(K_D)$ plot, which is consistent with the binding model³⁶.

Side specific inhibition with sybody. Although the analysis presented above is internally consistent, as well as consistent with existing kinetic data for binding on Glt_{ph}, there is a potential complication caused by the proteoliposome system used, because the reconstitution procedure usually results in a mix of inside-out- and right-side-out-oriented proteins in the bilayer. For instance, it has been demonstrated that Glt_{ph} reconstitutes in the two orientations with equal probability¹⁰. If the oppositely oriented proteins take up aspartate via different kinetic mechanisms (the equivalence of different mechanisms for forward and reverse transport *in vivo*), the results of the kinetic analysis could be convoluted and potentially lead to misinterpretation.

To determine to which extent the kinetic mechanism depends on the orientation of Glt_{Tk} in liposomes, we set out to inactivate either the right-side-out or the inside-out oriented transporters. Inhibition of the transporter from only one side of the membrane by modification of cysteine mutants did not work for Glt_{Tk}, possibly because of the one-gate nature of the elevator mechanism, in which the identical binding site residues and gating elements are alternately exposed to either side of the membrane¹³. Therefore, we chose to explore an alternative method by using synthetic nanobodies (sybodies)^{39,42}. Since sybodies recognize water-exposed surface epitopes and are membrane-impermeable, they are expected to be suitable for orientation-specific inhibition. We selected 42 unique sybodies against Glt_{Tk}, using an established platform, which included ribosome display, two rounds of phage display, and ELISA³⁹.

One of these sybodies (sybody 1) completely blocked aspartate transport by Glt_{Tk} when added from both sides of the membrane (in the lumen and in the external solution), but inhibited partially when added only on the outside of the proteoliposomes (Fig. 4a). It is important to note that the procedure to load sybodies in the liposome lumen includes an extrusion step in which all Glt_{Tk} molecules in the sample are exposed to the sybody. Therefore, it is not possible to do the opposite experiment, with the sybody exclusively included in the liposome lumen. Regardless of this limitation, the experiment conclusively showed that the sybody causes the sought-after sidedness of inhibition, and the result suggests that Glt_{Tk} had reconstituted in both orientations in the proteoliposomes, similar to what was shown for Glt_{ph} before. To explain the inhibitory properties of sybody 1, we solved a structure of the sybody-Glt_{Tk} complex using single-particle cryo-EM. The sybody binds on the extracellular surface of Glt_{Tk} at the interface between the transport and scaffold domain. The bound sybody thereby makes the elevator movement impossible, which prevents transport (Fig. 4b). The sybody thus inactivates the Glt_{Tk} molecules with right-side-out orientation, and the residual uptake activity can be attributed to the inside-out oriented proteins.

We chose to use this sybody, added only on the outside of the proteoliposomes, to repeat a subset of the experiments described above. First, we tested whether v_{max}^{Na} (app) still depended on the aspartate concentration and whether v_{max}^{Asp} (app) still depended on the Na⁺ concentration when the right-side-out oriented molecules were inactivated by the sybody. Indeed, both v_{max} (app) values still varied with the concentrations of the co-substrate (Fig. 4c, d), consistent with the kinetic mechanism (Eqs. (10) and (11)). Second, we determined whether a constant value for K_M^{r-Asp} (app) was still reached in the high Na⁺ concentration limit, as predicted by Eq. (13). Indeed, a constant value of ~0.6 μM was found above 100 mM Na⁺, which intriguingly did not deviate significantly from the value in the dual-population proteoliposomes (Table 5). Assuming that the k_{cat} value of the active population of inside-out oriented proteins was still ~0.9 s⁻¹, the value of k_3 remained unaltered. In other words, the measurable

parameters of the kinetic mechanism of the right-side-out and inside-out oriented proteins were very similar.

Discussion

Reconstitution of purified membrane proteins in liposomes often leads to mixed-orientation in lipid bilayers. For secondary active transporters, which can readily operate in both directions, the co-existence of right-side-out and inside-out oriented proteins is problematic for kinetic analysis. The work presented here shows that inactivation of transporter from one side of the membrane using a synthetic nanobody (sybody) is an effective way to deal with a mixed-orientation upon reconstitution in liposomes^{39,42}. Synthetic nanobodies are membrane impermeable, and highly specific for the binding epitope. While also natural nanobodies could be used for this purpose, sybodies offer a major advantage, because the selection can be carried out under defined buffer conditions, which may be used to steer the selection towards binders of a specific state. Also, the immobilization method used in the ribosome and phage display steps can be used to increase the chance of finding binders to the external or internal surface of the transporters. Finally, the generation of sybodies is quicker compared to nanobody generation, requires less protein, and does not require animal handling.

Here, the inactivation of the population of right-side out oriented Glt_{Tk} by sybody binding made it possible to analyze uptake catalyzed by inside-out oriented proteins. The aspartate transport rates obtained in the presence of the sybody can be compared directly with a previous pre-equilibrium binding study on detergent-solubilized Glt_{ph}. In the latter study, the transporter was fixed in the inward-oriented state by Hg²⁺-crosslinking of a double cysteine mutant, which allowed for the determination of the kinetic mechanism of binding of sodium ions and aspartate, and estimation of rate constants for association and dissociation³⁶. In our study, where we used a sybody to inactivate the population of right-side-out oriented Glt_{Tk} transporters in proteoliposomes, we measured the kinetics of the reversed transport step, which includes binding of Na⁺ and aspartate to the inward-oriented state similar to the pre-equilibrium binding study. In the Na⁺ concentration range between 5 and 300 mM, the two studies are fully congruent and consistent with a mechanism in which two sodium ions bind first, followed by aspartate, and finally the last sodium ion. The kinetic analysis presented here shows that the rate constant for association of aspartate (k_3 in Eq. (1)), can be obtained using Eq. (13) when K_M^{Asp} (app) is determined in the limit of high Na⁺ concentrations (as shown in Fig. 2) and the turnover number k_{cat} is taken directly from the maximally attainable rate at high Na⁺ and aspartate concentrations (v_{max}). The value for k_3 derived in this way was $1.3 \times 10^6 \text{ M}^{-1} \text{ s}^{-1}$, which closely matches the value of $1.2 \times 10^6 \text{ M}^{-1} \text{ s}^{-1}$ for Glt_{ph} derived from pre-equilibrium binding experiments³⁶.

More importantly, using the same analysis, it is also possible to determine the turnover number k_{cat} , if k_3 is known from binding experiments (which is the case for Glt_{ph}). This notion is relevant, because quantification of the amount of active transport protein present in membranes is often difficult, making a direct determination of k_{cat} from v_{max} values notoriously error-prone, which can be easily illustrated by the available data on Glt_{ph}. For aspartate transport by Glt_{ph}, the value for K_M^{Asp} (app) at 100 mM Na⁺ has been determined accurately (120 nM)⁴³. Assuming that this Na⁺ concentration is sufficiently high to represent the limit where K_M^{Asp} (app) has become constant and using the k_3 value of $1.2 \times 10^6 \text{ M}^{-1} \text{ s}^{-1}$ determined by pre-equilibrium binding, from Eq. (13) a k_{cat} value of 0.14 s^{-1} is calculated. This value has been derived without using the protein concentration.

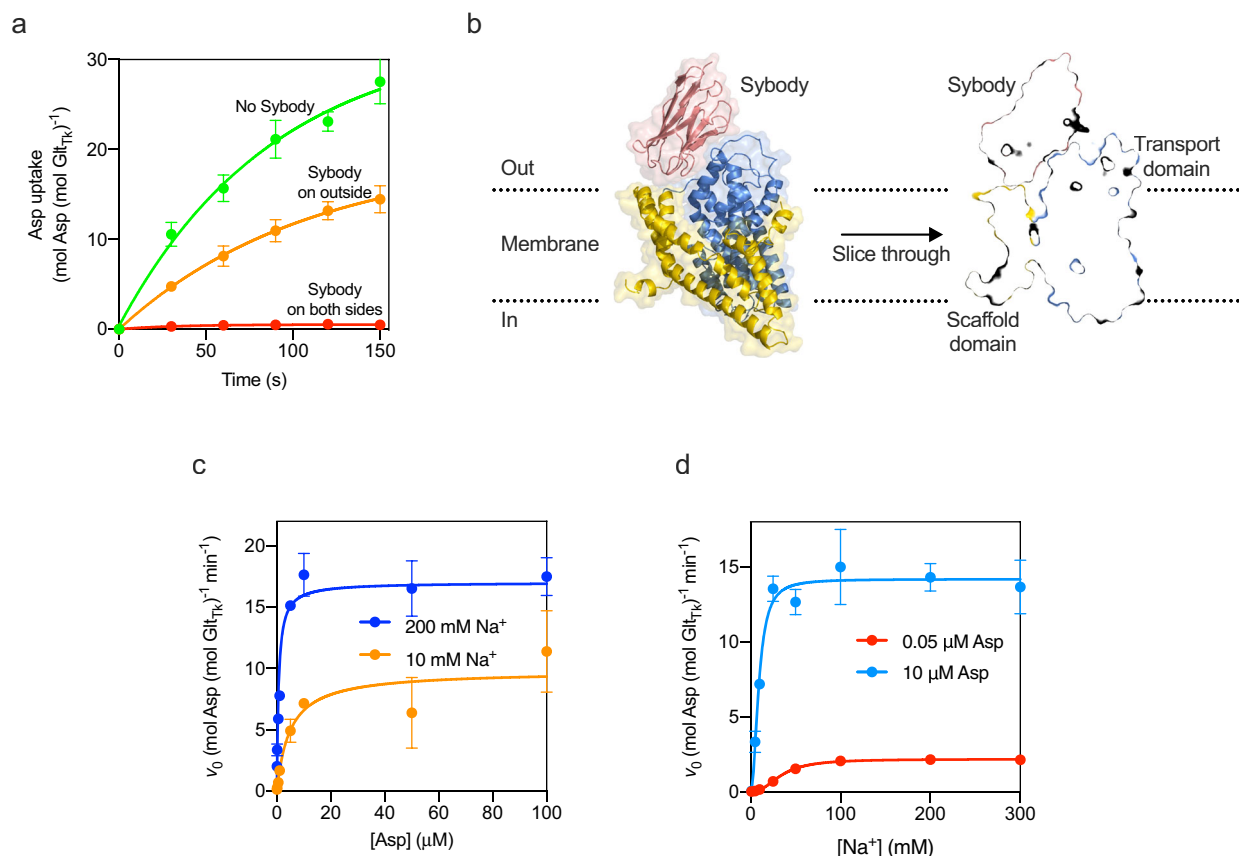


Fig. 4 Inhibition of aspartate transport by the sybody. **a** Uptake of aspartate in liposomes reconstituted with Glt_{TK} using aspartate and Na⁺ concentrations of 1 μM and 300 mM respectively. Uptake traces in the absence of sybody (green), in the presence of 750 nM sybody on the outside (orange), or with sybody present on both sides of the membrane (red). Each data point represents a triplicate measurement ($n = 3$), and the standard error of the mean is shown. **b** Cryo-EM structure of the Glt_{TK}-sybody complex. Left: cartoon representation of the Glt_{TK} protomer (transport domain in blue and the scaffold in yellow) that has the sybody bound (red). The surface of the protein is shown in transparent representation, and the approximate location of the membrane boundaries is indicated with dashed lines. Right: sliced-through representation highlighting that the sybody likely blocks movement of the transport domain along with the scaffold domain. The transport domain is in the intermediate-outward state, as described in ref. ¹³ **c, d** Same as in Fig. 1a, b for a selection of conditions (using the same color coding), but now in the presence of 750 nM sybody on the outside of the liposomes.

Table 5 Cryo-EM data collection, refinement, and validation.

Data collection and processing	
Voltage (kV)	200
Electron exposure (e ⁻ /Å ²)	53.3
Defocus range (μm)	-0.5 to -2.0
Pixel size (Å)	1.012
Symmetry imposed	C1
Initial dataset (# of particles)	109217
Final dataset (# of particles)	53983
Map resolution (Å) FSC _{0.143}	3.5
Refinement	
Initial model used	PDB 6XWQ
Model composition	
Nonhydrogen atoms	10357
Protein residues	1378
Ligands	3
Mean B factors (Å ²)	
Protein	160.2
Ligand	165.8
Rms deviations	
Bond lengths (Å)	0.005
Bond angles (°)	0.635
Validation	
MolProbity score	2.09
Clash score	17.7
Poor rotamers (%)	0.00
Ramachandran plot (%)	
Favored	95.07
Allowed	4.93
Outliers	0.00
Model to map fit CC	0.86

For comparison, if k_{cat} is derived directly from the v_{max} value of $3.4 \text{ nmol} \times \text{mg}^{-1} \times \text{min}^{-1}$, a value of $2.6 \times 10^{-3} \text{ s}^{-1}$ is found⁴³. The huge discrepancy between the two values is probably caused by inaccurate protein concentration determination in the proteoliposomes, or loss of activity during the reconstitution process.

It is noteworthy that in the experiments on Glt_{TK} presented here, the k_3 value of $1.3 \times 10^6 \text{ M}^{-1} \text{ s}^{-1}$ that we determined from the measurement of K_M^{Asp} (app) and k_{cat} was remarkably similar to the experimentally determined value of k_3 for Glt_{Ph} of $1.2 \times 10^6 \text{ M}^{-1} \text{ s}^{-1}$ ³⁶. The virtually identical rates of aspartate association step in Glt_{Ph} and Glt_{TK} are consistent with the structures of the binding sites in the two proteins, which are essentially the same^{7-9,13,15,16,20,44}. Therefore, we believe that the Glt_{TK} protein concentration, used to derive k_{cat} , was reasonably accurate in this case.

The sixfold difference in turnover number k_{cat} between Glt_{Ph} and Glt_{TK} (0.14 s^{-1} and 0.9 s^{-1} respectively) could be caused by (small) structural differences away from the binding site. k_{cat} is not a single rate constant but is composed of contributions from all steps that take place after binding of the last sodium ion in the catalytic cycle until the binding of the first sodium ion in the next round of catalysis. These steps include movement of the fully-loaded transport domain between outward- and inward-oriented states, the opening of the binding site towards the lumen of the liposomes, the release of the sodium ions and aspartate, occlusion

of the empty binding site in the apo-state, movement of the transport domain in the occluded apo-state, the opening of the binding site externally. The latter step also includes the rate constant for reshaping the binding sites for the first two sodium ions, leading to conformational selection that was shown to occur in Glt_{ph}³⁴. Therefore, differences between Glt_{ph} and Glt_{TK} that affect any of these steps may affect k_{cat} , which is observable in the value for K_M^{ASP} (app) at high sodium concentrations.

The origin of the differences between Glt_{ph} and Glt_{TK} may be similar to that of differences between wild-type Glt_{ph} and a faster “unlocked” mutant^{18,43}. This mutant has the same value for k_3 as the wild-type³⁶, consistent with the observation that the structure of the binding site is identical to the wild-type. Therefore, determination of K_M^{ASP} (app) in the limit of high sodium ion concentration allows for the derivation of accurate values for k_{cat} . The values for K_M^{ASP} (app) have been determined at 100 mM Na⁺ for both wild-type Glt_{ph} and the fast mutant (120 nM and 406 nM respectively)⁴³. If we again assume that this Na⁺ concentration is high enough to represent the limit where K_M^{ASP} (app) becomes constant for both proteins, then k_{cat} is predicted to be ~3.5 times higher in the fast mutant, which is in good agreement with bulk transport data that showed ~4.5 fold difference in v_{max} values (although the absolute numbers are both far off for the reasons discussed above)⁴³.

It is also possible to determine turnover numbers using a recently established transport assay at the single-molecule level⁴⁵, but combining turnover numbers from single-molecule transport measurements with rate constants determined in pre-equilibrium binding experiments is not straightforward. In pre-equilibrium binding experiments^{33,34,36,37} and bulk transport experiments (presented here), the entire ensemble contributes to the measured rate constants, and therefore data can be combined to describe the ensemble properties. In contrast, in single-molecule transport experiments, the k_{cat} is determined for only a fraction of the ensemble, and therefore it is difficult to quantitatively extract ensemble behavior, which would require accounting for the contribution of all subpopulations of (slightly) differently behaving individual proteins that together make up the ensemble⁴⁵. Conversely, ensemble measurements also cannot predict the single-molecule behavior, but the observation that the k_{cat} value determined by the ensemble measurements is lower than the maximal k_{cat} value determined in single-molecule measurements is consistent with the heterogeneity at the single-molecule level.

While the kinetic mechanism presented here is valid only for the reverse transport reaction (because we inactivated the forward-operating transporters by the sybody), it is well possible that the same mechanism is also used for the forward transport reaction. The similarity of the forward and reverse kinetic mechanisms is indeed supported by the essentially identical kinetic parameters in the presence and absence of the sybody. From a structural point of view, this similarity can be explained because the transporter uses the same gating element on both sides of the membrane (“one-gate elevator”), and the binding site geometry and access path in the inward- and outward-oriented states are essentially the same^{13,20,46,47}. In future experiments, the kinetic mechanism for forwarding transport by Glt_{TK} may be tested if we manage to inactivate the inside-out oriented population of Glt_{TK} molecules by a suitable sybody.

In contrast to what we found for Glt_{TK}, differences in the kinetic mechanisms of the forward and reverse reactions have been reported for the mammalian glutamate transporter EAAC1⁴⁸. The analysis of EAAC1 transport was based on the rapid-equilibrium assumption, which may be valid in this case, although it has not been tested systematically. Whether potential

mechanistic differences between the mammalian and archaeal transporters reflect evolutionary pressure to support different physiological needs is not clear. Alternatively, it is possible that the apparent differences in kinetic mechanism between Glt_{TK} and EAAC1 are caused by differences in the readout of transport. While transport was measured directly (using radioactivity) for Glt_{TK}, for EAAC1 the substrate-induced chloride conductance was used as a readout. In addition, different ranges of co-ion concentrations were used in the study of EAAC1 compared to the work presented here, which also may make the two studies not directly comparable.

In conclusion, analysis of the kinetic mechanism of sodium-coupled aspartate transport by Glt_{TK} and Glt_{ph} provides a way to determine accurate turnover numbers from K_M^{ASP} (app) values, without the need to use error-prone protein quantification. This is of great use for instance when analyzing the effects of mutations. Depending on the details of the kinetic mechanism, it may also be possible to determine turnover numbers in a similar way for other transport proteins. To test whether kinetic mechanisms different from the one analyzed here (Eq. (1)) would also allow for a similar determination of the turnover number, we used the King-Altman method^{38,41} to derive rate equations for all possible kinetic mechanisms leading to the coupled transport of three sodium ions and aspartate⁴⁰. It turns out that if at least one sodium ion binds after aspartate, K_M^{ASP} (app) values in the limit of high sodium concentration equal the ratio between k_{cat} and the on-rate for aspartate binding (as in Eq. (13)). It is also noteworthy that this even holds if multiple sodium ions bind randomly (for instance if steps 1 and 2 in Eq. (1) would be random). Therefore, it is likely that more transporters can be analyzed in the same way as presented here, and we conclude that systematic analysis of transport rates, and derivation of the rate equation, are essential steps in the elucidation of transport mechanisms.

Methods

Glt_{TK} purification and reconstitution in proteoliposomes. Glt_{TK} was produced in *Escherichia coli* strain MC1061 with the L-arabinose inducible vector pBad24 as described in Arkhipova et al.¹⁴. The cells were grown in LB media supplemented with 100 mg/L ampicillin. The expression was induced by the addition of 0.05% L-arabinose when the culture reached 0.8 OD₆₀₀. Three hours after induction the cells were harvested by centrifugation (7000 RPM, 15', 4 °C Beckman JLA 9.1000) and resuspended in ice-cold 20 mM Tris-HCl pH 8. The cells were lysed by means of a cell disruptor cooled to 4 °C and operated at 25 PSI. The lysate went through an intermediate centrifugation (7500 RPM, 20', 4 °C, Beckman JA25.50) step to remove cell debris, the supernatant was finally ultracentrifuged (40000 RPM 150', 4 °C, Beckman 50.1 Ti) and the pellet was resuspended in 20 mM Tris-HCl pH 8 before storing the membrane vesicles at –80 °C.

The membrane vesicles were then added to solubilization buffer (50 mM Tris-HCl pH8, 300 mM KCl, 1% DDM), incubated for 45' on a rocking platform at 4 °C, and finally centrifuged (55,000 RPM, 30', 4 °C, Beckman MLA 55) to separate the insoluble fraction from the solubilized protein. The supernatant was supplemented with 15 mM imidazole pH 8 and with 0.5 mL of Ni-Sepharose slurry pre-equilibrated with 50 mM Tris-HCl pH 8, 300 mM KCl. After 1 h of incubation the mixture was loaded onto a Poly-Prep column and unbound protein was allowed to flow through. The column was washed with 20 column volumes of washing buffer (50 mM Tris-HCl, 300 mM KCl, 60 mM imidazole, 0.15% DM) and finally eluted in three fractions of 300, 800, and 400 μ L respectively using elution buffer (50 mM Tris-HCl, 300 mM KCl, 500 mM imidazole, 0.15% DM). The second fraction was loaded onto a Superdex-200I gel filtration column equilibrated with 10 mM HEPES pH 8, 100 mM KCl and 0.15%DM. The final concentration of the purified protein was determined by measuring the absorbance at 280 nm (Glt_{TK} $\epsilon = 37,360$).

The lipids used to reconstitute Glt_{TK} contained a 3:1 mixture of *E. coli* lipid polar extract and egg phosphatidylcholine (PC) (Avanti). Liposomes were homogenized by extruding 11 times through a 400 nm pore size polycarbonate filter and subsequently diluted to 5 mg/mL in 50 mM potassium phosphate buffer (pH 7.0). To allow the insertion of the protein into the bilayer, the lipids were destabilized by step-wise addition of 10% Triton X-100 while scattering was followed at a wavelength of 540 nm. The titration was stopped once the absorption signal decreased to about 60% of the maximum value reached. Purified protein was added at a protein:lipid ratio (w/w) of 1:1600. The protein-lipid mixture was incubated for 30' at RT, and then the detergent was removed by addition of

BioBeads in three steps: First 15 mg/mL BioBeads were added followed by incubation for 60' at 4°C, then 19 mg/mL BioBeads were added followed by overnight incubation at 4°C. Finally, 29 mg/mL BioBeads were added followed by 120' incubation at 4°C. BioBeads were then removed and the proteoliposomes were pelleted (80,000 RPM, 25', 4°C, Beckman MLA80) and resuspended in 50 mM potassium phosphate buffer (pH 7) to a final lipid concentration of 20 mg/ml. The proteoliposomes were subjected to three cycles of freeze-thawing using liquid nitrogen and stored until use.

Sybody selection. Sybodies were selected against two Glt_{TK} cysteine mutants (298 C and 367 C), which while biotinylated and immobilized during the selection procedures would make extracellular and intracellular epitopes accessible for binding, respectively. Selection was done in the presence of 50 μM L-aspartate, 150 mM NaCl, and 0.15% DM according to an established in vitro selection platform that included ribosome display, two rounds of phage display, and ELISA (Zimmermann et al.^{39,42}). During ELISA, every single clone was analyzed for binding against Glt_{TK} in the presence and absence of L-aspartate. Sequencing of 48 ELISA positive hits resulted in 42 unique sybody sequences (20 for the 298 C mutant and 22 for the C367 mutant).

Sybody expression and purification. Each of 42 sybodies was expressed in *E. coli*, purified from the periplasm using Ni²⁺-affinity chromatography, and analyzed by size exclusion chromatography (SEC). Based on the quality of the SEC profiles (absence of aggregates, no interactions with column material, high yield) we selected 33 purified sybodies (14 for the 298 C mutant and 19 for the 367 C mutant), which were tested for their ability to inhibit Glt_{TK} transport of aspartate in uptake assays. For large scale purification of inhibitory sybody 1, a preculture of *E. coli* MCI1061 transformed with pSB_initSB1 was used to inoculate 50 mL of TB medium supplemented with 25 μg/ml chloramphenicol. The culture was grown for 2 h at 37°C while shaking at 200 rpm, the temperature was then lowered to 22°C and let grow until OD ~0.8. The expression was induced by adding L-arabinose to a final concentration of 0.02% and let express overnight at 22°C while shaking. Cells were pelleted and resuspended in 5 mL periplasmic extraction buffer (20% sucrose (w/v) 50 mM Tris-HCl (pH 8.0), 0.5 mM EDTA and 0.5 μg/ml lysozyme) and incubated on ice for 30 min, after incubation 20 mL of TBS (20 mM Tris-HCl (pH 7.4) 150 mM NaCl) supplemented with 1 mM MgCl₂ were added. The lysate was centrifuged at 4000 g for 20 min and the supernatant was transferred in a tube containing 500 μL of Ni-sepharose pre-equilibrated in TBS and supplemented with imidazole to a final concentration of 15 mM. After 1 h incubation on a shaking platform, the solution containing the SyBody was applied to a polyprep gravity column and the unbound fraction was let flow through. The resin was then washed with 10 CV of TBS supplemented with 30 mM imidazole and eluted in 500 μL of TBS supplemented with 300 mM imidazole. The sybody solution was then passed through a NAP-10 column equilibrated with the internal uptake buffer (10 mM potassium phosphate buffer (pH 7), 300 mM KCl) and stored at -80°C. Sybody 1 was selected from the library created by the mutant 298 C.

Transport assay. The luminal buffer in each proteoliposome preparation was changed to 10 mM potassium phosphate buffer (pH 7) and 300 mM KCl. For this, the proteoliposomes were first pelleted (80,000 RPM, 25', 4°C, Beckman MLA80) and then resuspended in the luminal buffer. After three freeze-thaw cycles, the suspension was extruded 11 times through a polycarbonate filter with 400-nm pore size in order to obtain homogeneously sized unilamellar vesicles which were pelleted (80,000 RPM, 25', 4°C, Beckman TLA100.3) and resuspended to a final lipid concentration of 100 mg/mL.

To completely inhibit aspartate transport of Glt_{TK} by sybody 1 (on both sides of the membrane) the luminal solution was supplemented with 150 μM of sybody 1. After performing 6 freeze-thaw cycles, and extrusion (11 times) through a polycarbonate filter with 400-nm pore size, the homogeneous solution was pelleted (80,000 RPM, 20', 4°C, Beckman TLA100.1) and resuspended to a final lipid concentration of 100 mg/mL in a solution containing 75 μM of sybody 1, 10 mM potassium phosphate buffer (pH 7) and 300 mM KCl.

To inhibit only the right-side-out fraction of Glt_{TK} a homogeneous solution of proteoliposomes was prepared as described above (with luminal buffer devoid of sybody) and after pelleting by ultracentrifugation it was resuspended to a final lipid concentration of 100 mg/mL with a solution containing 75 μM of sybody 1, 10 mM potassium phosphate buffer (pH 7) and 300 mM KCl.

To start the transport the proteoliposome suspension was diluted 100 fold into external buffer while stirring. The external buffer contained 10 mM potassium phosphate buffer (pH 7), 3 μM valinomycin, 1–300 mM NaCl, 0.05–100 μM L-aspartate; to balance the osmotic strength with that of the luminal solution, choline chloride was added (Table 1). In case the sybody was present, the 100-fold dilution resulted in a final external concentration of sybody of 750 nM.

After the indicated incubation period (20 s for the data in Figs. 1 and 4c, d), 2 mL of ice-cold quenching buffer (10 mM potassium phosphate (pH 7), 300 mM KCl) was added. The content of the tube was then poured onto a BA 45 nitrocellulose filter which was then washed with 2 mL of quenching buffer. The filters were finally dissolved in scintillation cocktail Ultima Gold (Perkin Elmer) and the β-decay from the radiolabeled substrate was counted. The time-point zero measurements for each condition was measured by pipetting the liposome

suspension on the side of a test tube containing 200 μL of reaction buffer and subsequently flushing them in the reaction buffer with 2 mL of ice-cold quenching buffer (10 mM potassium phosphate (pH 7), 300 mM KCl).

The value for each uptake rate represents the average and standard error of three independent biological replicates (different batches of expressed, purified, and reconstituted protein), each constituted by two or three technical replicates. The substrate-dependent uptake rates obtained at a fixed concentration of Na⁺ were plotted as a function of L-aspartate, and the Michaelis-Menten equation was fitted to the data to obtain apparent K_M (K_M^{ASP} (app)) and v_{max} (v_{max}^{ASP} (app)) values for different [Na⁺]. The co-ion-dependent uptake rates obtained at a fixed concentration of L-aspartate were plotted as a function of Na⁺, and the Hill equation was fitted to the data for obtaining K_M (K_D^{ASP} (app)), v_{max} (v_{max}^{Na} (app)), and n_{Hill} values for different [L-Asp]. The statistical analysis of the data was executed in GraphPad Prism 9.

Single particle Cryo-EM. The structure of Glt_{TK} in complex with sybody 1 (molar ratio 3:1) was determined using essentially the same protocol as described in Arkhipova et al.¹³, in the presence of 300 mM Na⁺ and 50 μM L-Asp. The purified complex at the concentration of 0.5–1 mg/ml was applied onto freshly glow-discharged Quantifoil grids (Au R1.2/1.3, 300 mesh) at 22°C and 100% humidity and plunged-frozen in liquid ethane. The Cryo-EM data were collected using 200-keV Talos Arctica microscope (Thermo Fisher). Cryo-EM image processing was performed using cryoSPARC software⁴⁹.

In brief, 824 micrographs were selected for the processing after motion correction and CTF estimation. The template for particle picking was generated from 100 manually picked particles. Template-based picking identified 109,217 particles. Subsequent 2D classification reduced the number of particles to 67,498 and subsequently 53,983 particles were left in the selected ab initio class. Final non-uniform 3D refinement resulted in a 3.5 Å map (with C1 symmetry applied), which was sharpened using Autosharpen Map procedure in Phenix⁵⁰ and used for model building using Coot⁵¹. The refinement of the coordinates was performed in the realspace refine module of Phenix⁵². The data collection and refinement statistics are shown in Table 5. Visualization and structure interpretation was carried out in UCSF Chimera⁵³ and PyMol (Schrodinger, LLC).

Statistics and reproducibility. Each uptake rate represents the average of three independent biological replicates (separate purifications and reconstitutions), each constituted by two technical replicates, and the standard error of the mean is shown in the figures and tables.

Reporting summary. Further information on research design is available in the Nature Research Reporting Summary linked to this article.

Data availability

Data supporting the findings of this manuscript are available from the corresponding authors upon reasonable request. A reporting summary for this Article is available as a Supplementary Information file. The source data underlying Figs. 1–4 and Tables 1–4 are provided as a Supplementary Data 1. The three-dimensional cryo-EM density map of the glutamate transporter homolog Glt_{TK} bound to the sybody has been deposited in the Electron Microscopy Data Bank under accession number EMD-12314 (<https://www.ebi.ac.uk/pdbe/emdb/>). Coordinates of the corresponding five models have been deposited in the Protein Data Bank under the accession number 7NGH (<https://www.rcsb.org/>).

Received: 23 February 2021; Accepted: 26 May 2021;

Published online: 17 June 2021

References

- Danbolt, N. C. Glutamate uptake. *Prog. Neurobiol.* **65**, 1–105 (2001).
- Kanner, B. I. & Sharon, I. Active transport of L-glutamate by membrane vesicles isolated from rat brain. *Biochemistry* <https://doi.org/10.1021/bi00612a011> (1978).
- Freidman, N. et al. Amino acid transporters and exchangers from the SLC1A family: structure, mechanism and roles in physiology and cancer. *Neurochem. Res.* <https://doi.org/10.1007/s11064-019-02934-x> (2020).
- Jensen, A. A., Fahlke, C., Bjørn-Yoshimoto, W. E. & Bunch, L. Excitatory amino acid transporters: Recent insights into molecular mechanisms, novel modes of modulation and new therapeutic possibilities. *Curr. Opin. Pharmacol.* **20**, 116–123 (2015).
- Zerangue, N. & Kavanaugh, M. P. Flux coupling in a neuronal glutamate transporter. *Nature* **383**, 634–637 (1996).
- Owe, S. G., Marcaggi, P. & Attwell, D. The ionic stoichiometry of the GLAST glutamate transporter in salamander retinal glia. *J. Physiol.* **577**, 591–599 (2006).

7. Yernool, D., Boudker, O., Jin, Y. & Gouaux, E. Structure of a glutamate transporter homologue from *Pyrococcus horikoshii*. *Nature* **431**, 811–818 (2004).
8. Jensen, S., Guskov, A., Rempel, S., Hänelt, I. & Slotboom, D. J. Crystal structure of a substrate-free aspartate transporter. *Nat. Struct. Mol. Biol.* **20**, 1224–1227 (2013).
9. Boudker, O., Ryan, R. M., Yernool, D., Shimamoto, K. & Gouaux, E. Coupling substrate and ion binding to extracellular gate of a sodium-dependent aspartate transporter. *Nature* **445**, 387–393 (2007).
10. Ryan, R. M., Compton, E. L. R. & Mindell, J. A. Functional characterization of a Na⁺-dependent aspartate transporter from *Pyrococcus horikoshii*. *J. Biol. Chem.* **284**, 17540–17548 (2009).
11. Kortzak, D. et al. Allosteric gate modulation confers K⁺ coupling in glutamate transporters. *EMBO J.* **38**, e101468 (2019).
12. Arkhipova, V. et al. Structural aspects of photopharmacology: insight into the binding of photoswitchable and photocaged inhibitors to the glutamate transporter homologue. *J. Am. Chem. Soc.* <https://doi.org/10.1021/jacs.0c11336> (2021).
13. Arkhipova, V., Guskov, A. & Slotboom, D. J. Structural ensemble of a glutamate transporter homologue in lipid nanodisc environment. *Nat. Commun.* **11**, 998 (2020).
14. Arkhipova, V. et al. Binding and transport of D-aspartate by the glutamate transporter homolog Glt_{TK}. *Elife* **8**, 1–12 (2019).
15. Guskov, A., Jensen, S., Faustino, I., Marrink, S. J. & Slotboom, D. J. Coupled binding mechanism of three sodium ions and aspartate in the glutamate transporter homologue Glt_{TK}. *Nat. Commun.* **7**, 1–6 (2016).
16. Reyes, N., Ginter, C. & Boudker, O. Transport mechanism of a bacterial homologue of glutamate transporters. *Nature* **462**, 880–885 (2009).
17. Georgieva, E. R., Borbat, P. P., Ginter, C., Freed, J. H. & Boudker, O. Conformational ensemble of the sodium-coupled aspartate transporter. *Nat. Struct. Mol. Biol.* <https://doi.org/10.1038/nsmb.2494> (2013).
18. Akyuz, N. et al. Transport domain unlocking sets the uptake rate of an aspartate transporter. *Nature* <https://doi.org/10.1038/nature14158> (2015).
19. Ruan, Y. et al. Direct visualization of glutamate transporter elevator mechanism by high-speed AFM. *Proc. Natl Acad. Sci. USA* **114**, 1584–1588 (2017).
20. Wang, X. & Boudker, O. Large domain movements through the lipid bilayer mediate substrate release and inhibition of glutamate transporters. *Elife* <https://doi.org/10.7554/eLife.58417> (2020).
21. Erkens, G. B., Hänelt, I., Goudsmits, J. M. H. H., Slotboom, D. J. & Van Oijen, A. M. Unsynchronised subunit motion in single trimeric sodium-coupled aspartate transporters. *Nature* **502**, 119–123 (2013).
22. Hänelt, I., Wunnicke, D., Bordignon, E., Steinhoff, H. J. & Slotboom, D. J. Conformational heterogeneity of the aspartate transporter Glt_{TPH}. *Nat. Struct. Mol. Biol.* **20**, 210–214 (2013).
23. Tanui, R., Tao, Z., Silverstein, N., Kanner, B. & Grewer, C. Electrostatic steps associated with substrate binding to the neuronal glutamate transporter EAAC1. *J. Biol. Chem.* **291**, 11852–11864 (2016).
24. Grewer, C. et al. Individual subunits of the glutamate transporter EAAC1 homotrimer function independently of each other. *Biochemistry* <https://doi.org/10.1021/bi050987n> (2005).
25. Leary, G. P., Stone, E. F., Holley, D. C. & Kavanaugh, M. P. The glutamate and chloride permeation pathways are colocalized in individual neuronal glutamate transporter subunits. *J. Neurosci.* <https://doi.org/10.1523/JNEUROSCI.4851-06.2007> (2007).
26. Koch, H. P., Brown, R. L. & Larsson, H. P. The glutamate-activated anion conductance in excitatory amino acid transporters is gated independently by the individual subunits. *J. Neurosci.* <https://doi.org/10.1523/JNEUROSCI.0118-07.2007> (2007).
27. Akyuz, N., Altman, R. B., Blanchard, S. C. & Boudker, O. Transport dynamics in a glutamate transporter homologue. *Nature* **502**, 114–118 (2013).
28. Stolzenberg, S., Khelashvili, G. & Weinstein, H. Structural intermediates in a model of the substrate translocation path of the bacterial glutamate transporter homologue GltPh. *J. Phys. Chem. B* **116**, 5372–5383 (2012).
29. Jiang, J., Shrivastava, I. H., Watts, S. D., Bahar, I. & Amara, S. G. Large collective motions regulate the functional properties of glutamate transporter trimers. *Proc. Natl. Acad. Sci. USA* <https://doi.org/10.1073/pnas.1112216108> (2011).
30. Groeneveld, M. & Slotboom, D. J. Rigidity of the subunit interfaces of the trimeric glutamate transporter GltT during translocation. *J. Mol. Biol.* **372**, 565–570 (2007).
31. Verdon, G. & Boudker, O. Crystal structure of an asymmetric trimer of a bacterial glutamate transporter homologue. *Nat. Struct. Mol. Biol.* <https://doi.org/10.1038/nsmb.2233> (2012).
32. Groeneveld, M. & Slotboom, D. J. Na⁺:aspartate coupling stoichiometry in the glutamate transporter homologue GltPh. *Biochemistry* **49**, 3511–3513 (2010).
33. Ewers, D., Becher, T., Machtens, J. P., Weyand, I. & Fahlke, C. Induced fit substrate binding to an archaeal glutamate transporter homologue. *Proc. Natl Acad. Sci. USA* **110**, 12486–12491 (2013).
34. Alleva, C. et al. Na⁺-dependent gate dynamics and electrostatic attraction ensure substrate coupling in glutamate transporters. *Sci. Adv.* **6**, eaba9854 (2020).
35. Reyes, N., Oh, S. & Boudker, O. Binding thermodynamics of a glutamate transporter homologue. *Nat. Struct. Mol. Biol.* **20**, 634–640 (2013).
36. Oh, S. & Boudker, O. Kinetic mechanism of coupled binding in sodium-aspartate symporter Glt_{TPH}. *Elife* **7**, 1–20 (2018).
37. Hänelt, I., Jensen, S., Wunnicke, D. & Slotboom, D. J. Low affinity and slow Na⁺ binding precedes high affinity aspartate binding in the secondary-active transporter Glt_{TPH}. *J. Biol. Chem.* **290**, 15962–15972 (2015).
38. Segel, I. H. Enzyme kinetics. in *Encyclopedia of Biological Chemistry: Second Edition* <https://doi.org/10.1016/B978-0-12-378630-2.00012-8> (2013).
39. Zimmermann, I. et al. Synthetic single domain antibodies for the conformational trapping of membrane proteins. *Elife* <https://doi.org/10.7554/eLife.34317> (2018).
40. Lolkema, J. S. & Slotboom, D. J. Models to determine the kinetic mechanisms of uncoupled transporters. *J. Gen. Physiol.* **151**, 369–380 (2019).
41. King, E. L. & Altman, C. A schematic method of deriving the rate laws for enzyme-catalyzed reactions. *J. Phys. Chem.* <https://doi.org/10.1021/j150544a010> (1956).
42. Zimmermann, I. et al. Generation of synthetic nanobodies against delicate proteins. *Nat. Protoc.* <https://doi.org/10.1038/s41596-020-0304-x> (2020).
43. Ryan, R. M., Kortt, N. C., Sirivanta, T. & Vandenberg, R. J. The position of an arginine residue influences substrate affinity and K⁺ coupling in the human glutamate transporter, EAAT1. *J. Neurochem.* <https://doi.org/10.1111/j.1471-4159.2010.06796.x> (2010).
44. Verdon, G., Oh, S. C., Serio, R. & Boudker, O. Coupled ion binding and structural transitions along the transport cycle of glutamate transporters. *Elife* **2014**, 1–23 (2014).
45. Ciftci, D. et al. Single-molecule transport kinetics of a glutamate transporter homologue shows static disorder. *Sci. Adv.* <https://doi.org/10.1126/sciadv.aaz1949> (2020).
46. Garaeva, A. A., Guskov, A., Slotboom, D. J. & Paulino, C. A one-gate elevator mechanism for the human neutral amino acid transporter ASCT2. *Nat. Commun.* <https://doi.org/10.1038/s41467-019-11363-x> (2019).
47. Garaeva, A. A. & Slotboom, D. J. Elevator-type mechanisms of membrane transport. *Biochem. Soc. Trans.* **48**, 1227–1241 (2020).
48. Zhang, Z. et al. Transport direction determines the kinetics of substrate transport by the glutamate transporter EAAC1. *Proc. Natl Acad. Sci. USA* **104**, 18025–18030 (2007).
49. Punjani, A., Rubinstein, J. L., Fleet, D. J. & Brubaker, M. A. CryoSPARC: Algorithms for rapid unsupervised cryo-EM structure determination. *Nat. Methods* <https://doi.org/10.1038/nmeth.4169> (2017).
50. Terwilliger, T. C., Sobolev, O. V., Afonine, P. V. & Adams, P. D. Automated map sharpening by maximization of detail and connectivity. *Acta Crystallogr. Sect. D Struct. Biol.* <https://doi.org/10.1107/S2059798318004655> (2018).
51. Emsley, P., Lohkamp, B., Scott, W. G. & Cowtan, K. Features and development of Coot. *Acta Crystallogr. Sect. D Biol. Crystallogr.* <https://doi.org/10.1107/S0907444910007493> (2010).
52. Afonine, P. V. et al. Real-space refinement in PHENIX for cryo-EM and crystallography. *Acta Crystallogr. Sect. D Struct. Biol.* <https://doi.org/10.1107/S2059798318006551> (2018).
53. Pettersen, E. F. et al. UCSF Chimera—a visualization system for exploratory research and analysis. *J. Comput. Chem.* <https://doi.org/10.1002/jcc.20084> (2004).

Acknowledgements

We thank Jan Rheinberger for help with cryo-EM sample preparation and data collection. This work was supported by the Dutch Research Council (NWO TOP grant 714.018.003 to DJS) and EMBO (short-term fellowship to AAG).

Author contributions

G.T. performed all experiments with the exception of the sybody selection (done by A.A. G. with help and supervision from C.A.J.H. and M.A.S.) and the cryo-EM sample preparation (done by V.A.) and structure determination (V.A. and A.G.). All authors designed experiments and analyzed data. D.J.S. and G.T. wrote the manuscript with input from all other authors.

Competing interests

The authors declare no competing interests.

Additional information

Supplementary information The online version contains supplementary material available at <https://doi.org/10.1038/s42003-021-02267-y>.

Correspondence and requests for materials should be addressed to D.J.S.

Peer review information *Communications Biology* thanks the anonymous reviewers for their contribution to the peer review of this work. Primary Handling Editors: Anam Akhtar. Peer reviewer reports are available.

Reprints and permission information is available at <http://www.nature.com/reprints>

Publisher's note Springer Nature remains neutral with regard to jurisdictional claims in published maps and institutional affiliations.



Open Access This article is licensed under a Creative Commons Attribution 4.0 International License, which permits use, sharing, adaptation, distribution and reproduction in any medium or format, as long as you give appropriate credit to the original author(s) and the source, provide a link to the Creative Commons license, and indicate if changes were made. The images or other third party material in this article are included in the article's Creative Commons license, unless indicated otherwise in a credit line to the material. If material is not included in the article's Creative Commons license and your intended use is not permitted by statutory regulation or exceeds the permitted use, you will need to obtain permission directly from the copyright holder. To view a copy of this license, visit <http://creativecommons.org/licenses/by/4.0/>.

© The Author(s) 2021